Structure of human ferroportin bound to hepcidin reveals mechanisms of iron homeostasis

Christian B. Billesbølle[1]*, Caleigh M. Azumaya[2]*, Rachael C. Kretsch[3-7], Alexander S. Powers[3-6,8], Shane Gonen[2,9,10], Simon Schneider[11], Tara Arvedson[12], Ron O. Dror[3-7], Yifan Cheng[2,9], Aashish Manglik[1,13]

[1]Department of Pharmaceutical Chemistry, University of California, San Francisco, 1700 4th Street, San Francisco, CA 94158, USA.
[2]Department of Biochemistry and Biophysics, University of California, San Francisco, 600 16th Street, San Francisco, CA 94158, USA.
[3]Department of Computer Science, Stanford University, Stanford, CA 94305, USA
[4]Department of Molecular and Cellular Physiology, Stanford University School of Medicine, Stanford, CA 94305, USA
[5]Department of Structural Biology, Stanford University School of Medicine, Stanford, CA 94305, USA
[6]Institute for Computational and Mathematical Engineering, Stanford University, Stanford, CA 94305, USA
[7]Biophysics Program, Stanford University, Stanford, CA 94305, USA
[8]Department of Chemistry, Stanford University, Stanford, CA 94305, USA
[9]Howard Hughes Medical Institute, University of California San Francisco, San Francisco, CA, USA
[10]Present address: Department of Molecular Biology and Biochemistry, University of California, Irvine, 2224 Biological Sciences III, Irvine, CA 92697, USA
[11]Institute of Biochemistry, Goethe University Frankfurt, Max-von-Laue-Straße 9, 60438 Frankfurt am Main, Germany
[12]Department of Oncology Research, Amgen Inc., South San Francisco, CA, United States
[13]Department of Anesthesia and Perioperative Care, University of California, San Francisco, 1700 4th Street, San Francisco, CA 94158, USA.

* These authors contributed equally
Correspondence to Yifan Cheng (Yifan.Cheng@ucsf.edu) or Aashish Manglik (Aashish.Manglik@ucsf.edu)

Abstract

The serum iron level in humans is tightly controlled by the action of the hormone hepcidin on the iron efflux transporter ferroportin. Hepcidin negatively regulates iron absorption and recycling by inducing ferroportin internalization and degradation. Aberrant ferroportin activity can lead to diseases of iron overload, like hemochromatosis, or iron limitation anemias. Here, we determined cryogenic electron microscopy (cryo-EM) structures of ferroportin in lipid nanodiscs, both in the apo state and in complex with cobalt, an iron mimetic, and hepcidin. These structures and accompanying molecular dynamics simulations identify two divalent metal binding sites within the N- and C-domains of ferroportin. Hepcidin binds ferroportin in an outward-open conformation and completely occludes the iron efflux pathway. The carboxy-terminus of hepcidin directly contacts the divalent metal in the FPN C-domain. We further show that hepcidin binding to ferroportin is coupled to iron binding, with an 80-fold increase in hepcidin affinity in the presence of iron. These results suggest a new model for hepcidin regulation of ferroportin, where only iron loaded ferroportin molecules are targeted for degradation. More broadly, our structural and functional insights are likely to enable more targeted manipulation of the hepcidin-ferroportin axis in disorders of iron homeostasis.

Introduction

Iron is essential for life. Complexed to heme, iron enables oxygen transport and cellular respiration. As a cofactor for many proteins, iron coordinates redox chemistry by alternating between ferrous (Fe^{2+}) and ferric (Fe^{3+}) oxidation states. Despite this central role in biology, free ferrous iron is toxic. In excess, iron can catalyze the production of free radicals, leading to cellular damage. Iron levels are therefore tightly controlled, both at the cellular and organism level.

In mammals, iron levels are regulated by the action of hepcidin, a peptide hormone, on ferroportin (FPN), the only known iron efflux transporter[1–3] (Fig. 1a). FPN mediates absorbance of dietary iron by transport of ferrous iron across the basolateral surface of intestinal enterocytes. FPN also mediates iron recycling from hepatocytes and macrophages[4]. Iron efflux by FPN is controlled by the amount of transporter located at the cellular surface. FPN synthesis is transcriptionally regulated by cellular hypoxia, iron and heme concentrations, and inflammatory signaling[5]. In settings of elevated serum iron levels, liver-derived hepcidin levels increase and this hepcidin negatively regulates cell surface FPN by acutely blocking iron transport[6] and inducing FPN ubiquitination, internalization, and degradation[7–10]. Hepcidin activity decreases serum iron levels by suppressing FPN-mediated dietary iron absorption and release of iron from cellular stores.

Iron disorders in humans can result from dysregulation of hepcidin or FPN, reflecting the central role of the hepcidin-FPN axis in iron homeostasis. Deficits in hepcidin-mediated regulation of FPN, often due to hereditary hemochromatoses, lead to iron overload and widespread tissue damage affecting the liver, pancreas, and joints[11–13]. By contrast, inappropriate elevation of hepcidin levels yields iron-restricted anemia[14,15]. Although several approaches to restore aberrant FPN function have been evaluated in clinical trials[16–18], none have thus far succeeded.

The molecular mechanism of FPN regulation by hepcidin remains incompletely defined at the atomic level. A confluence of human genetics studies and structure-function evaluations have identified key regions of FPN important in hepcidin regulation[6,19–22]. A key recent advance was determination of the X-ray crystal structure of a divalent metal transporter from the bacterium *Bdellovibrio bacteriovorus* (bbFPN) with 40% similarity to human FPN[23,24], which revealed a unique architecture among the broader major facilitator superfamily (MFS) of membrane

transporters. Although bbFPN is predicted to share structural features with human FPN, the precise mechanisms of iron coordination likely differ and bbFPN is not regulated by hepcidin.

To understand how FPN transports iron, and how this process is regulated by hepcidin, we used a combination of cryogenic electron-microscopy (cryo-EM), molecular dynamics simulations, and *in vitro* biochemical assays. These studies reveal the molecular recognition of iron and hepcidin by FPN and suggest a new regulatory mechanism enabling hepcidin to selectively target actively transporting ferroportin molecules for degradation.

Structures of apo- and hepcidin-bound human FPN

We screened the antigen-binding fragments (Fabs) of antibodies previously raised against FPN[25] for use as a fiducial mark to guide image alignment of a small membrane protein embedded in a lipid nanodisc for structure determination by single particle cryo-EM, a strategy we proposed many years ago[26]. Among the many Fabs that bound purified FPN (Supplementary Fig. 1), a single clone, Fab45D8, yielded interpretable class averages in negative stain EM and was selected to facilitate cryo-EM structure determination. Unlike many antibodies and antibody fragments targeting FPN, Fab45D8 was previously determined to be non-competitive with hepcidin and, on its own, did not induce FPN internalization[25]. Indeed, in nanodisc-reconstituted preparations of FPN, Fab45D8 did not alter the binding properties of hepcidin (Supplementary Fig. 2).

We determined cryo-EM structures of nanodisc-reconstituted FPN bound to Fab45D8, both in the apo state (3.2 Å, Supplementary Fig. 3) and bound to hepcidin and Co^{2+} (2.5 Å, Supplementary Fig. 4). We independently validated prior reports that FPN transports cobalt[27] (Supplementary Fig. 1). Unlike Fe^{2+}, Co^{2+} is not readily oxidized and therefore provides a tractable surrogate divalent metal for FPN biochemical and structural studies. The cryo-EM density map of FPN enabled building of an atomic model of FPN regions important for iron transport and hepcidin binding[1,6], and a portion of the intracellular loop 3 (ICL3) important in hepcidin-induced FPN internalization[8–10](Supplementary Fig. 3 and 5a & Supplementary Table 1). The entire FPN extracellular loop 5 (ECL5) remains unresolved, likely due to significant conformational flexibility. To enable modeling of Fab45D8, we separately obtained its X-ray crystal structure at 2.1 Å (Supplementary Fig. 6 and Supplementary Table 2)

Both cryo-EM structures reveal a monomeric FPN bound to a single Fab45D8 molecule, which recognizes a short alpha helical segment in FPN extracellular loop 2 (ECL2) (Fig. 1b and Supplementary Fig. 6). Similar to other MFS transporters, FPN contains twelve transmembrane (TM) helices arranged in two domains (Fig. 2a). Both the N-terminal and C-terminal domains are composed of six helices, with a large central cavity that, in both apo- and hepcidin-bound structures, is open to the extracellular side and closed intracellularly (Fig. 2b). Ferroportin shares significant structural similarity with the bacterial bbFPN transporter, with an overall root mean squared deviation (RMSD) of 2.0 Å when compared to the outward-open conformation of bbFPN (Fig. 2c). The overall backbone conservation is even higher within the isolated C-terminal domain (RMSD 1.4 Å). Unlike most other MFS transporters, the alpha helix of FPN TM7 is interrupted by a short non-helical stretch of six residues. This unique feature, previously posited to be important in iron binding[24], is shared between FPN and bbFPN.

Several interacting residues define an intracellular gate that keeps the N- and C- domains of FPN in an outward open conformation. Similar to a previously observed interaction network in bbFPN[23], R489 in TM11 of the C-domain forms an ionic interaction with D157 in TM4 of the N-domain (Fig. 2d). This interaction is further supported by an extended ionic and hydrogen-bonding network including residues E486 (TM11) and R88 (TM3). In FPN, an additional cluster of ionic and hydrogen bonding interactions between TM5 in the N-domain and TM10 in the C-domain further stabilizes the outward open conformation (Fig. 2e). Mutation of several residues within the intracellular gate leads to FPN loss of function in ferroportin disease, highlighting the importance of the gate in coordinating the conformational steps necessary for iron efflux[19,28].

Iron binds to the N and C domains of FPN

Two distinct sites capable of binding divalent cations have previously been proposed for bbFPN. Although initial crystallographic studies suggested that iron primarily binds in a cavity within the N domain of the bbFPN transporter[23], further mutagenesis studies found a critical divalent cation binding site within the C domain[24]. Structural elucidation of the FPN iron binding site, however, remains elusive. Previous studies on bbFPN either used supraphysiological concentrations of iron or found Ni^{2+} bound as an EDTA complex.

We obtained cryo-EM data for a Co^{2+}-hepcidin-FPN complex in the presence of a 8-fold molar excess of $CoCl_2$ to FPN (100 μM $CoCl_2$:12.5 μM FPN) to minimize artifacts arising from supraphysiological metal concentrations. Comparison of this map with the apo-FPN map revealed two new densities in the central cavity of FPN, corresponding to single metal binding sites in the N and in the C domain respectively (Fig. 3a-c). Within the C domain, Co^{2+} directly interacts with C326 in TM7b and H507 in TM11 while making a water-mediated contact with D325 and the backbone carbonyl of T320 (Fig. 3b). Intriguingly, the tetrahedral coordination geometry for Co^{2+} is fulfilled by the carboxy terminus of hepcidin. Within the N domain, we observe density for Co^{2+} coordinated directly by TM1 residues D39 and H43 (Fig. 3c).

We captured Co^{2+} bound to FPN in the presence of hepcidin. Hepcidin binding likely influences the structure and dynamics of FPN and it is therefore possible that the metal binding sites are different in FPN in the absence of hepcidin. To better understand divalent metal binding to FPN in the absence of hepcidin, we used all-atom molecular dynamics simulations. We first performed six simulations of apo-FPN in a hydrated lipid bilayer with Fe^{2+} ions initially positioned randomly in bulk solvent. In all six independent simulations, Fe^{2+} ions bound spontaneously to the C domain, localizing to the unwound region of TM7 near residues D325, D504, and H507 within hundreds of nanoseconds of simulation time (Fig. 3d and Supplementary Fig. 7). The Fe^{2+} ion also occasionally moves closer to TM1 to interact with D39, consistent with the additional N-domain site observed in the hepcidin-bound structure. In parallel simulations of apo-FPN run without Fe^{2+} ions, we observed mobility of TM7b, with significant fluctuations of D325 (Fig. 3e). This observation is consistent with comparatively weaker cryo-EM density for TM7b as compared to other transmembrane helices in apo-FPN (Supplementary Fig. 7). By contrast, both D325 and TM7b are less mobile in simulations with iron bound at the C domain site (Fig. 3e). Divalent metal binding to the C domain may therefore stabilize an otherwise dynamic TM7b in a conformation that favors hepcidin-binding.

The identification of two metal binding sites within FPN raises the question of whether both sites are required for iron efflux. Several human FPN mutations that lead to hereditary hemochromatosis map to residues that directly coordinate Co^{2+} in the C domain, including C326S/F/Y[13,29–31] and H507R[32]. Although these mutations likely disrupt the precise coordination geometry required for metal binding, they are fully competent to transport iron even in the presence of hepcidin; indeed, this lack of hepcidin-responsiveness leads to iron overload.

Mutation of D325 leads to decreased iron efflux[22], which initially suggested a key site for iron efflux in the C domain of FPN[24]. However, recent modeling studies of an inward open conformation of FPN based on bbFPN suggest that D325 may interact with the N domain; loss of iron efflux in D325 mutants may therefore be caused by disruption of the extracellular gate[33]. By contrast, mutation of D39 to alanine in the N domain metal binding site of FPN completely abolishes iron efflux from HEK293 cells[22], suggesting that the N domain may be a primary site for effluxed iron. Because the C domain metal-binding site is important for hepcidin binding, it may primarily serve an important iron-dependent regulatory function in hepcidin control of FPN activity.

Hepcidin occludes outward open FPN

Hepcidin binds FPN in a central cavity between the N and C domains, acting as a molecular cork to completely occlude the iron efflux pathway (Fig. 1c and 4a). This structural observation supports recent studies demonstrating acute inhibition of iron transport by hepcidin that is independent of FPN ubiquitination and degradation[6]. Although the conformations of apo- and Co^{2+}-hepcidin-bound FPN are highly similar (RMSD 0.73 Å), the Co^{2+}-hepcidin-bound structure shows a ~3 Å rigid body separation of the N and C domains on the extracellular side of FPN (Fig. 4b). Within the N domain, hepcidin binding leads to displacement of TM2 from the central cavity, driven in part by a specific contact between I6 of hepcidin and T61 and Y64. Within the C domain, the largest conformational changes occur around the Co^{2+} binding site, leading to changes in the conformation of TM7b and the extracellular side of TM11 (Fig. 4b).

Hepcidin makes extensive polar and hydrophobic contacts with FPN with a total buried surface area of ~1300 $Å^2$. Our structure of hepcidin bound to FPN provides insight into disease-causing mutations associated with FPN gain of function in hereditary hemochromatoses. Several FPN mutations decrease hepcidin binding to FPN, including N144H/D/T[34–36], C326S/F/Y[13,29–31], Y333H[37], Y501C[6,38], D504N[6,39] and H507R[32]. Of these, C326 and H507 directly coordinate the cobalt ion and mutations therefore indirectly affect hepcidin affinity or alter the atomic basis of binding specificity. Other interactions between FPN and hepcidin are either hydrophobic or depend on hepcidin amide backbone atoms, which is consistent with the relatively high tolerance of amino acid substitutions within hepcidin[40]. For example, Y333 fits into a hydrophobic cavity in hepcidin and hydrogen bonds with the backbone carbonyl of hepcidin residue M21 (Fig. 4c). D504 in FPN coordinates the backbone amide of hepcidin H3 while Y501

π-stacks with the imidazole side chain of H3 (Fig. 4c). A further hydrogen bond between N144 and Y501 further stabilizes this interaction network. In contrast to these mutations, the Y64N/H mutants retain hepcidin binding[6], but are completely resistant to hepcidin-induced FPN ubiquitination[41,42]. The outward displacement of TM2 near Y64 induced by hepcidin may therefore be important for FPN ubiquitination (Fig. 4c).

The structure of hepcidin bound to FPN provides insight into prior efforts to engineer hepcidin mimetics as potential therapeutics for diseases of iron overload[20,40,43,44]. Although the first two residues of hepcidin (DT) are dispensable for activity, residues 3-8 (HFPICI) are absolutely required for function[20]. Indeed, the first two residues of hepcidin make minimal interactions with FPN (Fig. 4c). By contrast, alanine scanning mutagenesis suggested an important role for hydrophobic hepcidin residues including F4 and F9, and to a lesser extent H3 and I6[40,43,44]. Residues F4 and F9 insert between the N and C domains of FPN at opposite ends of the central cavity (Fig. 4c); hydrophobic residues at these positions likely stabilize the FPN outward open state. More unexpected is the extensive set of contacts between hepcidin residues 10-25 and TM7b of FPN. Prior studies have recapitulated hepcidin activity with a linear peptide composed of hepcidin residues 1-9, though with a ~8-20 fold reduction in potency[40,45]. Whether these minihepcidins fully plug the iron efflux pathway remains unclear. Furthermore, in the absence of structural data, it remains unclear whether minihepcidin variants coordinate divalent metals in the same manner as observed for hepcidin in our structure.

In addition to blocking the iron transport pathway, hepcidin regulates FPN by causing ubiquitination of lysine residues in intracellular loop 3 (ICL3)[9,10]. Among these, K240 is critical for hepcidin-induced FPN internalization and degradation. Neither the apo- or Co^{2+}-hepcidin-bound structures resolve residues 239-288 of ICL3, precluding a structural understanding of how hepcidin regulates the conformation of K240. In the resolved regions of ICL3, we observe no significant conformational changes between apo- and Co^{2+}-hepcidin-bound FPN (Fig. 4d,e). Several caveats may limit our structural analysis of hepcidin-induced conformational changes in FPN, including the lack of a membrane voltage or proton gradient across the lipid nanodisc, the requirement for specific lipids for FPN function, or other cofactors important in hepcidin-induced FPN ubiquitination. However, the structures provide clues into the role of ICL3 in FPN function. The N terminal portion of ICL3 (residues 230-238) forms interactions with the N domain (Fig. 4d). Notably, K236 makes an ionic interaction with the intracellular gate residue D157. The C

terminal portion of ICL3 (residues 291-304) forms an amphipathic helix that makes a number of contacts with both TM2 in the N domain and TM11 in the C domain, which both undergo conformational changes upon binding hepcidin (Fig. 4e). In both cases, the resolved regions of ICL3 are primed to sense the conformation of the transporter as it shuttles iron and binds hepcidin. These regions may therefore serve as important conduits linking the conformation of hepcidin binding on the extracellular side to K240 conformation on the intracellular side.

Hepcidin is coupled to iron binding

The direct interaction between hepcidin and Co^{2+} in our structure is unexpected (Fig. 5a), and suggests that divalent metals may be important for hepcidin binding to FPN. We therefore directly tested the effect of Fe^{2+} and Co^{2+} on hepcidin affinity at FPN. A fluorescently tagged version of hepcidin (Rhodamine green-hepcidin[25], RhoG-Hep) bound to nanodisc-reconstituted ferroportin with an apparent K_D of 210 nM (pK_D = -6.67± 0.02) (Fig. 5b). In the presence of 10 μM $FeCl_2$, we observed a significantly increased affinity of 2.5 nM (pK_D = -8.61 ± 0.21), an almost 80-fold change in the potency of hepcidin at FPN. Addition of $CoCl_2$ also increased hepcidin affinity. Consistent with a cooperative effect, the effect of $CoCl_2$ on hepcidin binding was saturable (Fig. 5c).

The reference range for hepcidin concentration in healthy adults is ~1-30 nM[46]. Our *in vitro* binding experiment with purified FPN indicates minimal hepcidin binding to FPN in the absence of a divalent metal, suggesting that metal binding to FPN may regulate hepcidin activity *in vivo*. Our structure of FPN bound to Co^{2+} and hepcidin revealed conformational changes in TM7b associated with hepcidin binding (Fig. 3e) and a direct contact between hepcidin and Co^{2+}(Fig. 3b); both could be important for the observed effect of Fe^{2+} and Co^{2+} on hepcidin binding. We therefore tested whether disruption of the C domain iron binding site influences hepcidin binding. Even in the presence of 50 μM $CoCl_2$, the D325N, C326S, and H507R mutants bound hepcidin weakly, titrating in a micromolar range similar to wild-type FPN in the absence of divalent metals (Fig. 5c). These results highlight the critical role of the C domain metal site in potent hepcidin binding to FPN, which is likely important in homeostatic control of iron levels in a physiological setting.

Discussion

Ferroportin is a central regulator of iron homeostasis in humans. Both human FPN and the bacterial homologue bbFPN show remarkable similarities in their overall architecture, with a unique conformation of TM7 responsible for molecular recognition of iron within the C domain. This similarity suggests a deep evolutionary history for FPN-like transporters within the broader major facilitator superfamily. Hepcidin, by contrast, is specific to vertebrates and likely evolved as a new strategy to regulate a critical point in iron absorption. The structures presented here map, at high resolution, metal and hepcidin binding to FPN.

We determined that hepcidin binding to FPN is greatly potentiated by iron itself, potentially due to the stabilizing effect iron has on the hepcidin-binding site of FPN (Fig. 5d). With iron, the binding affinity of hepcidin falls in a range concordant with the concentration of hepcidin observed in healthy human adults. In normal iron homeostasis, this may enable hepcidin to selectively bind and regulate FPN molecules actively transporting iron and loaded with Fe^{2+}, while sparing FPN molecules located on cells with low transport activity. Hepcidin binding to FPN would both trap the transporter in an outward open state and limit iron egress; both actions acutely decrease iron efflux, as has been recently reported[6]. Elevated hepcidin levels likely inappropriately overcome this regulatory strategy and degrade FPN even in the absence of active iron efflux. The potentiation of hepcidin activity by iron may therefore have immediate consequences for the development of hepcidin mimetics currently in clinical trials[16]. Furthermore, hepcidin antagonism by direct targeting of FPN may require molecules with high potency to overcome the nanomolar effect of the hormone in the presence of iron. The structural and functional insights into FPN function presented here therefore provide critical foundations for the discovery of therapeutics for human disorders of iron homeostasis.

MAIN TEXT FIGURES

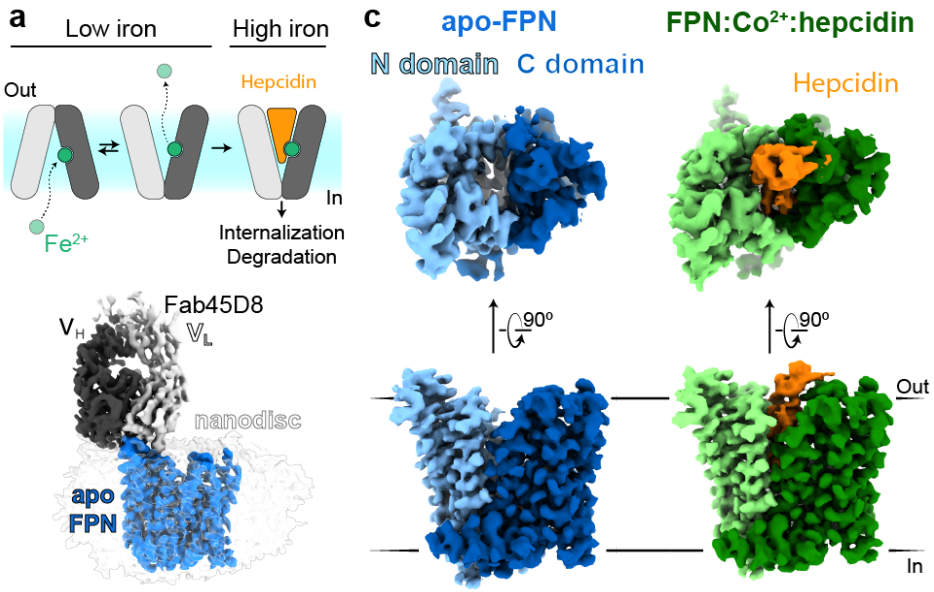

Figure 1. Structures of human ferroportin. a, Ferroportin effluxes cellular iron (Fe^{2+}) by an alternating access mechanism. Hepcidin binds to outward open ferroportin and induces ubiquitination and degradation. **b,** Cryo-EM map of apo-FPN-Fab45D8 complex in lipid nanodisc. **c,** Cryo-EM density of apo and Co^{2+}/hepcidin bound FPN. The N and C domains are colored in different shades of blue for apo-FPN and green for Co^{2+}/hepcidin bound FPN. Hepcidin (orange) binds to an extracellular facing cavity in FPN.

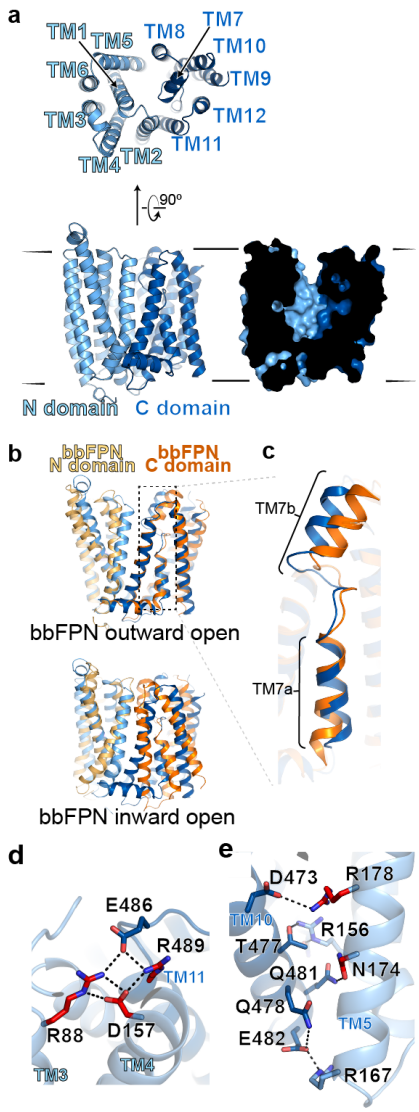

Figure 2. Structure of apo-FPN and similarity to bbFPN. a, Ribbon diagram of FPN reveals 12 transmembrane helices. The N- and C-domains are colored in different shades of blue. Cutaway surface view (right) shows outward open conformation. **b,** Human FPN aligned to the outward-open (PDB: 5AYN) and inward-open (PDB: 5AYO) conformations of bbFPN. **c,** Unique architecture of TM7 shared between human FPN and bbFPN. **d,** Intracellular gating residues are shown as sticks. Residues in red are known FPN loss-of-function mutations **e,** TM10 and TM5 form an extensive network of interactions, further stabilizing the outward open conformation. Residues highlighted in red are known loss-of-function mutations that lead to ferroportin disease in humans.

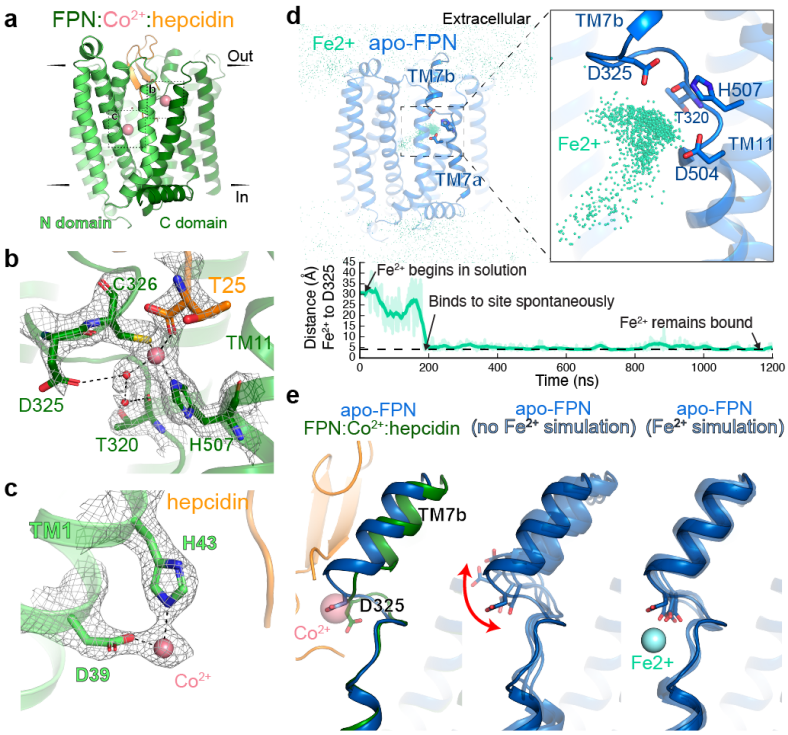

Figure 3. Iron binds to the N and C domains of FPN. a, Ribbon diagram of FPN-Co^{2+}-hepcidin complex. Hepcidin binds an extracellular-facing pocket in FPN. **b,** Closeup view of cryo-EM density for Co^{2+} ion in the FPN C domain. Co^{2+} binds with tetrahedral coordination to C326, H507, a water molecule, and the hepcidin C-terminus. **c,** Closeup view of cryo-EM density for Co^{2+} ion in the FPN N domain, coordinated by H43 and D39. **d,** In molecular dynamics simulations with Fe^{2+} initially positioned randomly in bulk water surrounding FPN, the Fe^{2+} ions spontaneously bind to a region near H507, D325, and D504. The aggregated position of Fe^{2+} ions from six simulations, each 2 μs in length, is shown superimposed with apo FPN. **c,** In one representative simulation, an Fe^{2+} ion spontaneously binds within 200 ns and remains localized at this site for more than 1000 ns. Distance shown is from the ion to the nearest oxygen atom of the D325 side chain. Thick trace represents a 15-ns sliding mean and thin traces represent unsmoothed values**. e,** Comparison of TM7b conformation in apo-FPN and FPN bound to Co^{2+} and hepcidin. In simulations without Fe^{2+}, TM7b is dynamic, with significant fluctuation of D325. D325 coordinates Fe^{2+} in simulations, and is associated with decreased TM7b motion.

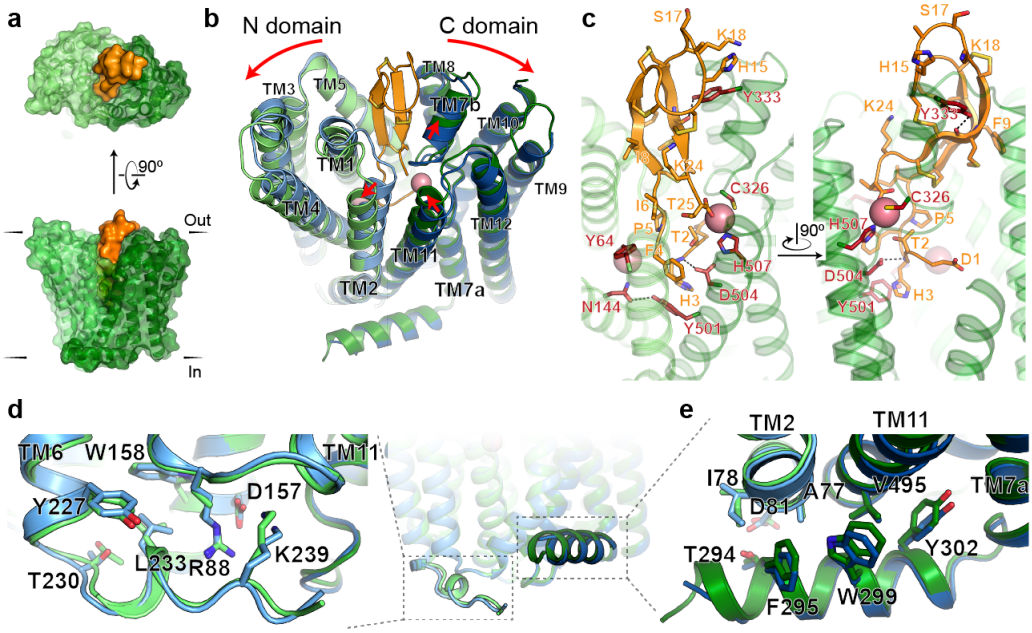

354

355 **Figure 4. Hepcidin binding to FPN. a,** Surface representation of the FPN-Co^{2+}-hepcidin
356 complex viewed from the extracellular side and perpendicular to the membrane plane. **b,**
357 Ribbon diagrams of apo-FPN (blue) aligned to FPN-Co^{2+}-hepcidin (green, orange, and pink
358 spheres) showing the overall separation of the N and C domains, and the displacement of TMs
359 containing key residues for hepcidin binding. **c,** Close-up views of the hepcidin binding site.
360 Residues in red are known hepcidin resistance mutations involved in ferroportin disease. **d,e**
361 Close-up of interactions between the transmembrane regions and intracellular loop 3.

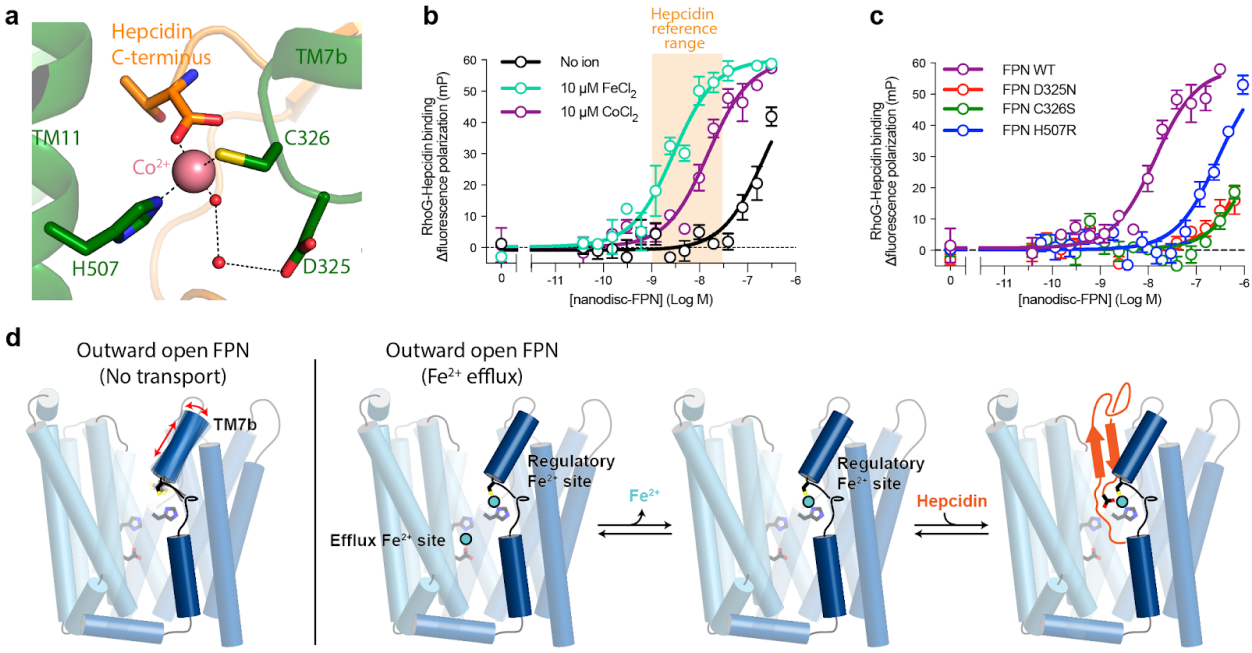

Figure 5. Hepcidin binding is potentiated by iron. a, FPN C domain metal binding site. Shown are residues that interact with Co^{2+}, including D325, C326, and H507 in FPN as well as the hepcidin C-terminus. **b,** Fluorescence polarization increase in rhodamine green-labeled hepcidin (RhoG-hepcidin) as nanodisc-reconstituted FPN is titrated with a K_D of 210 nM. Addition of 10 μM $FeCl_2$ or $CoCl_2$ increases the affinity of hepcidin to 2.5 nM and 7.7 nM (pK_D = -8.11 ± 0.16), respectively. Hepcidin concentration range in healthy human adults is shown in orange. **c,** Mutation of the C domain metal binding sites decreases RhoG-hepcidin binding affinity at FPN, even in the presence of 50 μM $CoCl_2$. All values are reported as mean ± s.e.m. Error bars represent s.e.m. **d,** Model for iron-coupled hepcidin regulation of FPN function. In settings of iron efflux, TM7b is conformationally stabilized by iron coordination in the C domain regulatory site. High affinity hepcidin binding to outward open FPN depends on the direct coordination of iron in the C domain.

METHODS

No statistical methods were used to predetermine sample size. The experiments were not randomized and the investigators were not blinded to allocation during experiments and outcome assessment.

Expression and purification of human ferroportin

The wild-type human FPN gene was cloned into a pVL1392 vector containing an expression cassette comprised of a C terminal human rhinovirus 3C (HRV-3C) protease recognition sequence followed by a human protein C epitope tag (EDQVDPRLIDGK) and an 8x polyhistidine tag. Baculovirus was generated using *Spodoptera frugiperda* Sf9 insect cells (unauthenticated and untested for mycoplasma contamination, Expression Systems 94-001F) and the construct was expressed in *Spodoptera frugiperda* Sf9 insect cells. Cells were collected 48 h after transduction and stored at −80°C until further use. Frozen cell pellets were thawed and washed with a hypotonic buffer (20 mM HEPES pH 7.50, 1 mM EDTA, supplemented with 20 µg/mL leupeptin, and 160 µg/mL benzamidine) before solubilizing with 50 mM HEPES pH 7.5, 300 mM NaCl, 1% (w/v) n-dodecyl-β-D-maltopyranoside (DDM, Anatrace), 0.1% (w/v) cholesteryl hemisuccinate (CHS, Steraloids), 1 mM EDTA supplemented with 20 µg/mL leupeptin, and 160 µg/mL benzamidine for 1 h at 4°C. Following centrifugation, the resulting supernatant was loaded on homemade anti-protein C antibody Sepharose beads and washed extensively in 50 mM HEPES pH 7.50, 300 mM NaCl, 2 mM $CaCl_2$, 0.1% (w/v) DDM, 0.01% (w/v) CHS. FPN was eluted with 50 mM HEPES pH 7.50, 300 mM NaCl, 0.1% (w/v) DDM, 0.01% (w/v) CHS, 0.2 mg/mL Protein C peptide (Genscript) and 5 mM EDTA. The protein was concentrated with a Vivaspin 100-kDa MWCO concentrator and the monomeric FPN fraction was collected after size-exclusion chromatography (SEC) over a Superdex S200 Increase 10/300 GL column (GE Healthcare) equilibrated with 20 mM HEPES pH 7.50, 100 mM NaCl and 0.1% (w/v) DDM, and 0.01% (w/v) CHS.

Expression and purification of MSP

Constructs encoding MSP-NW9 or MSP-NW11[47] in the pET28b vector (Addgene #133442) were transformed into BL21(DE3) Rosetta *Escherichia coli*, and grown in terrific broth medium supplemented with 2 mM $MgCl_2$ and 0.1% (w/v) glucose at 37°C. At OD_{600} of ~0.6, expression was induced by addition of 400 µM isopropyl β-d-1-thiogalactopyranoside (IPTG) and lowering the temperature to 20°C. Cells were harvested after 16 hours and resuspended into 5 mL lysis

buffer (200 mM Tris pH 8.0, 500 mM NaCl, 1% (v/v) Triton X-100 (Sigma), 0.02 mg/mL leupeptin, 0.16 mg/mL benzamidine, and benzonase) per gram pellet. After stirring for 30 min at 4°C, cells were lysed by pulsed sonication on ice. The lysate was cleared by centrifugation at 15,000 x g for 25 min at 4°C and loaded on Ni-NTA Sepharose. Ni-NTA beads were washed with 50 mM Tris pH 8.0, 500 mM NaCl, 1% (v/v) Triton, then 50 mM Tris pH 8.0, 500 mM NaCl, 50 mM sodium cholate, then 50 mM Tris pH 8.0, 500 mM NaCl, and finally with 50 mM Tris pH 8.0, 500 mM NaCl, 30 mM Imidazole. MSP was eluted with 50 mM Tris-HCl pH 8.0, 500 mM NaCl, 400 mM Imidazole and dialyzed into 50 mM Tris–HCl, pH 8.0, 100 mM NaCl, 1 mM EDTA, 0.1 mM TCEP at 4°C. The following day, MSP was concentrated on a Vivaspin 10-kDa MWCO concentrator, aliquots were flash frozen in liquid nitrogen and stored at -80°C for reconstitution.

Isolation, expression and purification of Fab45D8

The heavy and light chain sequences of mAb45D8[25] were separately cloned into pcDNA3.4 and the resulting vectors were transfected into Expi293F Human Embryonic Kidney cells (Life Technologies) using a 1:2 mass ratio of light and heavy chain DNA with the Expifectamine transfection kit (Life Technologies) as per the manufacturer's instructions. Supernatant containing mAb45 was harvested 136 h after transfection and loaded on homemade Protein G Sepharose beads and extensively washed with a buffer comprising 20 mM HEPES pH 7.50, and 100 mM NaCl. mAb45D8 was eluted with 100 mM glycine (pH 3.0) and fractions were immediately neutralized with 200 mM HEPES pH 7.50. To generate the Fab fragment, 10 mg of purified mAb45D8.1 was diluted into 9.5 ml freshly prepared cleavage buffer (20 mM sodium phosphate pH 7.00, 10 mM EDTA, and 10 mM cysteine) and treated with 0.5 ml agarose immobilized papain (Thermo Scientific) at 37°C. After 16 h the cleaved Fab45D8 fragment was purified by reverse Protein A affinity chromatography, followed by SEC into buffer comprising 20 mM HEPES pH 7.50 and 100 mM NaCl. Fab45D8 was concentrated on a Vivaspin 10-kDa MWCO concentrator, and aliquots were flash frozen in liquid nitrogen and stored at -80°C for later use.

Reconstitution of FPN into lipidic nanodisc

Purified FPN (0.2-0.5 mg) was mixed with purified MSP and a lipid mixture containing a 2:3 weight ratio of 1-palmitoyl-2-oleoylphosphatidylcholine (POPC, Avanti) and 1-palmitoyl-2-oleoyl-sn-glycero-3-phospho-(1'-rac-glycerol) (POPG, Avanti). For reconstitution

into NW9 nanodiscs, an FPN:MSP:Lipid molar ratio of 1:20:1100 was used. For reconstitution into NW11 nanodiscs, an FPN:MSP:Lipid molar ratio of 1:20:800 was used. The reconstitution sample was nutated for 1 h at 4°C before addition of 0.2 g/mL SM2-BioBeads (BioRad), and the reconstitution sample was further nutated overnight at 4°C before removal of the biobeads. FPN containing nanodiscs were purified by loading the reconstitution sample on anti-protein C antibody Sepharose beads and washing extensively with 20 mM HEPES pH 7.50, 100 mM NaCl, and 1 mM $CaCl_2$ to remove empty nanodiscs. FPN containing nanodiscs were eluted with 20 mM HEPES pH 7.50, 100 mM NaCl, 0.25 mM EDTA, and 0.2 mg/mL Protein C peptide (Genscript), and concentrated on a Vivaspin 50-kDa concentrator.

Crystallization and structure determination of Fab45D8

Purified Fab45D8 was diluted to 13.0 mg/mL in 20 mM HEPES pH 7.5, 100 mM NaCl. Fab45D8 crystals were obtained in 0.3 M trimethylamine-N-oxide (TMAO), 0.1 M Tris pH 8.5, and 30% (w/v) PEG 2000 MME at 20 °C. Individual crystals were flash frozen in liquid nitrogen after a 30 s soak in 0.3 M trimethylamine-N-oxide (TMAO), 0.1 M Tris pH 8.5, and 30% (w/v) PEG 2000, and 20% v/v ethylene glycol. A full diffraction dataset was collected at the Advanced Photon Source GM/CA-CAT beamline 23ID-B, and processed using xia2dials[48] implementation of XDS[49]. The structure of the Fab was solved by molecular replacement using Phaser[50], with a search model of a closely related germline mouse monoclonal antibody (PDB ID: 6BZV[51]) lacking complementarity determining regions (CDRs). The model was iteratively improved by refinement in Coot[52] and Phenix[53]. Data collection and refinement statistics are summarized in Supplementary Table 1. The final model contained 96.77%, 2.23% and 0% in the favored, allowed and outlier regions of the Ramachandran plot, respectively as assessed by MolProbity[54].

Calcein transport assay for divalent cations

FPN was reconstituted into liposomes for divalent cation transport assays. Empty liposomes were prepared as a 3:1 mass ratio of 1-palmitoyl-2-oleoyl-sn-glycero-3-phosphoethanolamine (POPE, Avanti) to POPG dissolved in chloroform, followed by gentle evaporation of the chloroform under a stream of nitrogen gas, and overnight desiccation. The lipids were dissolved in 20 mM HEPES pH 7.40, 100 mM KCl to a final concentration of 12.5 mg/mL, sonicated until optically clear, subjected to multiple freeze-thaw cycles, and extruded through a 400 nm polycarbonate filter (Avestin) to generate unilamellar vesicles. Subsequently 0.13% (w/v)

Triton-X100 (Sigma) was added to destabilize liposomes, corresponding to the concentration yielding 80% of the maximum OD_{540} obtained in a liposome destabilization curve. Purified FPN was added at a 1:50 protein to lipid mass ratio and incubated for 15 min at 4°C. Control liposomes devoid of FPN were prepared in parallel using the same concentration of DDM. To remove excess detergent, 0.05 g/mL of SM2-BioBeads were added to the sample and nutated for 1 hr at 4°C, then 0.05 g/mL SM2-BioBeads were added followed by incubation overnight at 4°C, and finally addition of 0.08 g/mL SM2-BioBeads followed by incubation for 2 hr at 4°C. Proteoliposomes were harvested by ultracentrifugation at 300,000 x g for 30 min and resuspended at a concentration of 2.0 mg/mL lipids in internal buffer comprised of 20 mM HEPES pH 7.40 and 100 mM KCl, before flash freezing in liquid nitrogen and storage at -80°C. On the day of the transport assay, proteoliposomes were thawed and incubated with 500 mM calcein (Sigma), then subjected to three freeze-thaw cycles, and extruded through a 400 nm polycarbonate filter. The liposomes were washed four times with external buffer comprising 20 mM HEPES pH 7.40 and 100 mM NaCl, by repeated ultracentrifugation and resuspension. Immediately prior to the assay, the calcein containing proteoliposomes were diluted to 0.25 mg/mL lipid in external buffer. Time-course fluorescence traces were recorded as 1 s integrations using a FluoroMax-4 (Horiba) with λ_{ex} of 490 nm and λ_{em} of 520 nm. Steady state fluorescence was recorded for at least 5 min, before addition of small aliquots of freshly prepared stocks of either $FeCl_2$ or $CoCl_2$. To stabilize the ferrous (Fe^{2+}) state, we prepared iron as a 1:10 ratio of sodium ascorbate:$FeCl_2$ immediately prior to the experiment. To determine the full extent of the calcein quenching response, 10 μM of the divalent cation ionophore calcimycin (Sigma) was added at the end of each experiment. Transport data was normalized to the mean baseline fluorescence intensity prior to addition of ion.

Hepcidin binding assays

Fluorescence polarization measurements were performed using rhodamine-green labeled hepcidin (RhoG-hepcidin)[25]. For FPN saturation binding experiments, samples were prepared in a black 384-well plate (Greiner) containing 0-1 μM of nanodisc reconstituted NW11-FPN and 5 nM RhoG-hepcidin in sample buffer comprising 20 mM HEPES pH 7.50, 100 mM NaCl, and supplemented with $FeCl_2$, $CoCl_2$ or $MnCl_2$ as indicated. For ion stimulation experiments, 100 nM NW11-FPN and 5 nM RhoG-Hepcidin was mixed with 0-600 μM of $CoCl_2$. For Fab binding experiments, 100 nM NW11-FPN and 5 nM RhoG-Hepcidin was mixed with 0 - 3 μM of Fab45D8 in sample buffer containing 10 μM $CoCl_2$. Binding reactions were equilibrated for 60

min at RT, and fluorescence polarization was recorded on a Biotek Synergy H4 (Agilent) in polarization mode using fixed bandpass filters with λ_{ex} of 484 nm and λ_{em} of 520 nm.

Analytical fluorescence size exclusion chromatography (FSEC) was performed by mixing 25 µg of NW11-FPN with 2 x fold molar excess of RhoG-Hepcidin in sample buffer comprised of 20 mM HEPES (pH 7.50), 100 mM NaCl and 10 µM $CoCl_2$. Samples were incubated for 20 min on ice and 1.5 x molar excess of Fab45D8, or sample buffer, was added followed by incubation for 30 min on ice. For homologous competition, 1 µM NW11-FPN was mixed with 30 µM unlabelled hepcidin (Bachem) in sample buffer comprised of 20 mM HEPES (pH 7.50), 100 mM NaCl and 10 µM CoCl, and incubated for 30 min on ice. Then 2 µM RhoG-Hepcidin was added and the sample incubated for 30 min on ice. Samples were injected on a Superdex 200 Increase 10/300 GL column (GE Lifesciences) pre-equilibrated in 20 mM HEPES pH 7.50, 100 mM NaCl, and 10 µM $CoCl_2$. RhoG-Hepcidin fluorescence was recorded using an FP-1520 Intelligent Fluorescence Detector (Jasco) with λ_{ex} of 493 nm and λ_{em} of 524 nm.

Cryo-EM Sample Preparation and Data Collection

Nanodisc-reconstituted apo-FPN was mixed with 1.15 molar excess of Fab45D8 and incubated on ice for 30 min. The complex was purified by size-exclusion chromatography over a Superdex S200 Increase 10/300 GL column (GE Healthcare) equilibrated with 20 mM HEPES pH 7.50, 100 mM NaCl. For Co^{2+}/hepcidin samples, 600 µM $CoCl_2$ and 30 µM hepcidin (Bachem) was added to nanodisc-reconstituted FPN and incubated for 20 minutes on ice prior to addition of Fab45D8. The resulting complex was purified over size-exclusion chromatography as for the apo sample but with the addition of 100 µM $CoCl_2$ in the chromatography buffer. Collected fractions were supplemented with fresh hepcidin to 30 µM. For both preparations, fractions containing the nanodisc-FPN-Fab45D8 complex were concentrated to ~3 mg/ml on a Vivaspin 50-kDa MWCO concentrator and freshly used for electron microscopy.

For high-resolution cryo-EM, the apo-FPN-Fab45D8 complex was diluted to 0.0375 mg/mL in 20 mM HEPES pH 7.5, 100 mM NaCl directly prior to vitrification, and 2 µL sample was applied to glow-discharged gold holey carbon 1.2/1.3 300-mesh grids (Quantifoil) coated in-house with graphene oxide[55–57]. Grids were blotted for 2-4 seconds at 0 force and 10 seconds wait time before being plunge vitrified in liquid ethane using a MarkIV Vitrobot (ThermoFisher). The blotting chamber was maintained at 22°C and 100% humidity during freezing.

Co^{2+}/hepcidin samples were diluted to 1.5 mg/mL in gel filtration buffer (20 mM HEPES pH 7.5, 100 mM NaCl, 100 μM $CoCl_2$) before vitrification. Grids were blotted for 3 seconds at 0 force and 5 seconds wait time before being plunge vitrified in liquid ethane using a MarkIV Vitrobot (ThermoFisher). The blotting chamber was maintained at 22°C and 100% humidity during freezing.

FPN-Fab45D8 and Co2+/hepcidin-FPN-Fab45D8 movies were collected using a Titan Krios (ThermoFisher) outfitted with a K3 camera and Bioquantum energy filter (Gatan). The K3 detector was operated in superresolution mode and the energy filter slit width was set to 20 eV. Movies were collected at a nominal magnification of 105,000x, physical pixel size 0.834Å/pix, with a 70 μm C2 aperture and 100 μm objective aperture at a dose rate of 8 e^-/pixel/second. A total dose of 66 $e^-/Å^2$ was collected as a 120-frame movie, resulting in a 6-second movie with 0.55 e^-/frame. Data were collected using semi-automated imaging scripts in SerialEM[58]. For FPN-Fab45D8, 5009 movies were collected using a 3x3 image shift pattern at 0º tilt and 406 movies were collected on-axis with a 30º stage tilt in two separate data collection sessions. For Co2+/hepcidin-FPN-Fab45D8, 4395 movies were collected at 0° tilt in a single data collection session.

Cryo-EM Image Processing

For FPN-Fab45D8, data were motion corrected and 2x binned on-the-fly using MotionCor2[59] in the SCIPION pipeline[60]. Motion corrected micrographs were imported into cryoSPARC[61] and RELION[62] and contrast transfer function parameters were calculated using CTFFIND4[63]. CTF information for tilted images were estimated using patch CTF estimation in cryoSPARC. 138,314 particles were selected from 497 micrographs using the Blob picker in cryoSPARC. 2D class averages were generated after extracting the putative particles with a 300-pixel box and binning to 64 pixels. Six of these averages were used as templates for further particle picking. Template picking yielded 4,737,795 particles. These were split into 6 groups to increase speed of processing, extracted in a 300-pixel box, and binned to 64 pixels. 2D classification was run in cryoSPARC with default settings except: number of 2D classes 200, initial classification uncertainty factor 4, number of online-EM iterations 40, batch size per class 300. Objectively “good” (showing clear Fab and receptor density) class averages were selected and exported to RELION format using csparc.py[64]. Class averages that were not classified as “good”, but were

not clearly ice contamination or graphene oxide edges, were run through a second round of 2D classification with default settings except: number of 2D classes 200, number of online-EM iterations 40, batch size per class 300. All “saved” class averages from the second rounds of 2D classification in cryoSPARC selected and exported to RELION format using csparc.py. Particles were extracted from CTF-corrected images in RELION at a box size of 300 pixels, binned to 128 pixels. 1,326,130 particles, in three groups (detailed in Supplementary Fig. 3) were classified in 3D with image alignment in RELION using an initial model generated in cryoSPARC from 80,000 particles collected on a Talos Arctica filtered to 40 Å, C1 symmetry, a regularization parameter of 4, for 30-35 iterations with no mask. Particles from classes with resolved transmembrane (TM) helices were selected, extracted in a 300-pixel box, and imported back into cryoSPARC. Non-uniform refinement was run with default settings and no resolution limit, resulting in angle and shift assignments for 850,000 particles. These particles were subsequently exported to RELION format using csparc.py and run through 3D classification without image alignment in RELION. Four of the 12 classes were selected, imported into RELION, run through non-uniform alignment with an automatically generated mask, and refined to a reported global resolution of 3.2 Å. The resulting map showed clear signs of mild preferred orientation (Supplementary Fig. 3). The particles were exported into RELION format using csparc.py, converted into an image stack, and imported into cisTEM[65] as a refinement package. The particles were reconstructed and half-maps were generated using the “generate 3D” command. These half-maps, as well as the half-maps from cryoSPARC were run through our lab’s directional Fourier shell correlation (dFSC) program[66] clearly showing a more distributed range of views in the map generated by cisTEM. Maps were sharpened in RELION. Resolutions are reported using the FSC = 0.143 cut-off[67] and were estimated in cryoSPARC and cisTEM.

For Co^{2+}/hepcidin-FPN-Fab45D8, data were motion corrected and 2x binned on-the-fly using MotionCor2[59] in the SCIPION pipeline[60]. Motion corrected micrographs were imported into cryoSPARC[61] and contrast transfer function parameters were calculated using CTFFIND4[63]. 3,753,516particles were selected from 4395 micrographs using the template picker in cryoSPARC with 2D averages from the apo-FPN dataset as templates. These particles were extracted in a 360-pixel box, and binned to 64 pixels. 2D classification was run in cryoSPARC with default settings except: number of 2D classes 200, initial classification uncertainty factor 4, number of online-EM iterations 40, batch size per class 300. Objectively “good” (showing clear Fab and receptor density) class averages were selected for 3D classification. Class averages

that were not classified as “good”, but were clearly not ice contamination, were run through a second round of 2D classification with default settings except: number of 2D classes 200, number of online-EM iterations 40, batch size per class 300. All “saved” class averages from the second rounds of 2D classification in cryoSPARC were sent to 3D classification. These particles were subjected to two rounds of heterogeneous refinement in cryoSPARC that serves as a “trash collector”. Four initial models were used, three generated from an early round of ab initio model generation and our final apo-FPN-Fab45D8 structure. All initial models were filtered to 30Å before refinement. Particles were unbinned and a final heterogeneous refinement was performed with three good initial models of apo-FPN-Fab45D8. Non-uniform refinement was run with default settings and no resolution limit, on the most populated class resulting in angle and shift assignments for 310,647 particles. The particles were exported into RELION format using csparc.py, converted into an image stack, and imported into cisTEM[65] as a refinement package. The particles were reconstructed and half-maps were generated using the “generate 3D” command. These half-maps, as well as the half-maps from cryoSPARC were run through our lab’s directional Fourier shell correlation (dFSC) program[66] clearly showing a more distributed range of views in the map generated by cisTEM. Maps were sharpened in cisTEM. Resolutions are reported using the FSC = 0.143 cut-off[67] and were estimated in cryoSPARC and cisTEM.

Model building and refinement

For apo-FPN, a homology model of human FPN in the outward open state was built using Modeller[68], with a previously determined X-ray crystal structure of outward open bbFPN (PDB ID: 5AYN)[23] as a template. After truncating putatively flexible regions (N-terminus, ICL3, ECL5, and C-terminus), the resulting model was fit into the 3.2 Å cryo-EM map of FPN:Fab45D8 using Chimera[69]. The initial template was manually rebuilt in Coot[52] and iteratively refined with real space refinement implemented in Phenix[53]. Model geometry was assessed using MolProbity[54]. Further validation was performed with EMRinger[70] to compare the map and final model. Map-to-model FSCs were calculated within Phenix. Figures were prepared in Chimera[69] and PyMol.

To dock hepcidin into the Co^{2+}/hepcidin-bound and apo-FPN difference density, we used a previously determined X-ray crystal structure of hepcidin bound to a neutralizing Fab as a starting model[21]. Hepcidin, without the first two residues, was manually placed within the difference density in Coot, then real-space refined to conform to the difference density

with maintaining the disulfide connectivity and secondary structure observed in the starting model. The resulting model docked to FPN has an overall RMSD of 1.2 Å compared to the starting model for regions with defined secondary structure.

Molecular dynamics simulations

The structure of the outward-open apo conformation of human FPN was used as the starting coordinates for all simulations. Three different conditions were simulated (Supplementary Table 3): (1) the iron-absent condition, where no iron was added; (2) the iron-bound condition, where an Fe^{2+} ion was placed in the proposed iron binding site 5.6 Å from D325 α-carbon, 6.9 Å from D504 α-carbon, and 7.8 Å from H507 α-carbon; (3) the iron-in-bulk-solvent condition, where 15 Fe^{2+} ions were placed randomly in the water box outside the protein using Dabble[71].

Simulation coordinates were prepared by removing non-FPN molecules from the initial structure. Prime (Schrödinger) was used to model missing side chains, and neutral acetyl and methylamide groups were added to cap protein termini. The unresolved loops between TM6-TM7 and TM9-TM10 (residues 239-290 and 394-451 respectively, inclusively) were not modeled. The termini surrounding these loops were capped. PropKa was used to determine the dominant protonation state of all titratable residues at pH 7[72,73]. The structure was internally hydrated using Dowser[74]. Dabble was used to additionally fill the extracellular cavity[71]. The structure was aligned using the Orientation of Proteins in Membranes (OPM) server[75].

Using Dabble, the protein was inserted into a pre-equilibrated 1-palmitoyl-2-oleoylphosphatidylcholine (POPC) membrane bilayer. For all simulations except condition three (iron in bulk solvent), sodium and chloride ions were added at 150 mM to neutralize the system. For condition three, chloride ions were added to neutralize the system resulting in a concentration of 108 mM. A periodic box was used with dimensions 90 x 90 Å in the x-y plane and a water buffer of 10 Å above and below the protein to the periodic boundary. We used the CHARMM36m parameters for lipids, proteins, sodium and chloride ions, and the TIP3P model for waters[76–78]. The Fe^{2+} Lennard-Jones parameters were obtained from Li *et. al.'s* compromise model[79].

All simulations were run on a single Graphical Processing Unit (GPU) using the Amber18 Compute Unified Device Architecture (CUDA) version of particle-mesh Ewald molecular

dynamics (PMEMD)[80,81]. For each condition, 6 replicates were run. For each independent replicate, the system was minimized with 500 steps of steepest descent followed by 500 steps of conjugate gradient descent three times. 10 and 5 kcal mol^{-1} $-Å^2$ harmonic restraints were used on the protein, lipid, and Fe^{2+} ions for the first and second minimization, respectively. 1 kcal mol^{-1} $-Å^2$ harmonic restraints were used on the protein and Fe^{2+} ions for the final minimization. The system was then heated from 0 K to 100 K over 12.5 ps in the NVP ensemble with a Langevin thermostat and harmonically restraining the protein heavy atoms and Fe^{2+} ions with a restraint of 10 kcal mol^{-1} $-Å^2$. The system was further heated with the same restraints from 100 K to 310 K in the NPT ensemble over 125 ps. The system was equilibrated with harmonic restraints on protein heavy atoms and Fe^{2+} ions for 30 ns. The restraint strength started at 5 kcal mol^{-1} $-Å^2$ and was reduced by 1 kcal mol^{-1} $-Å^2$ every 2 ns for the first 10 ns and then by 0.1 kcal mol^{-1} $-Å^2$ every 2 ns for the final 20 ns. Production simulations were performed at 310 K and 1 bar using the NPT ensemble, a Langevin thermostat and a Monte Carlo barostat. Every 200 ps snapshots were saved. All simulations were run for at least 2.2 μs. These simulations used a 4-fs time step with hydrogen mass repartitioning[82]. Bond lengths to hydrogen atoms were constrained using SHAKE[82,83]. Non-bonded interactions were cut off at 9 Å.

Simulation Analysis Methods

MD snapshots were reimaged every 1 ns and centered using CPPTRAJ package in AmberTools18[84]. Simulations were visualized using Visual Molecular Dynamics and figures prepared in PyMOL[85]. Time traces from simulation were smoothed using a moving average with a window size of 15 ns unless otherwise indicated and visualized with the PyPlot package from Matplotlib. For all analysis in the manuscript that required structural alignment, we aligned to the initial Ferroportin structure using the backbone atoms of residues 26-116, 127-228, 308-483, and 492-543.

To investigate the localization of Fe^{2+} ions, the iron-in-bulk-solvent simulations (condition 3) were analyzed. To visualize the density of Fe^{2+} ions, the position of Fe^{2+} ions was recorded every 10 ns for each of the 6 simulation replicates, each 2 μs in length. Each Fe^{2+} ion position was then drawn as a point superimposed on the starting structure (Fig. 3d). To quantify the binding events, the distance between iron and the closest side chain oxygen atom on D325 was measured. This distance was graphed over 1.2 μs, including the equilibration time (Fig. 3d).

To investigate the dynamics and conformation of the TM7b region, the iron-absent (condition 1) and iron-bound (condition 2) simulations were compared. The TM1-TM7b distance was measured using distance between the Cα of V51 and the Cα of Y333. For each simulation, we calculated the average of the distance over 2.2 μs, excluding equilibration. The average over the simulations for each condition was plotted with error bars representing the standard error of the mean (s.e.m.) (Supplementary Fig. 7). The dynamics of D325 were also investigated. The dynamics were visualized by overlaying representative frames showing the movement of D325, the binding site, and TM7b. For iron-absent simulations, frames from a single replicate at 200, 350, 500, and 550 ns were overlaid (Supplementary Fig. 7). For iron-bound simulations, frames from a single replicate at 200, 500, 725, 1000 ns were overlaid (Supplementary Fig. 7). The conformational range of D325 was quantified by measuring the distance between Cγ of D325 and Cβ of S47. This was visualized for one replicate for each condition over a time of 1 μs inclusive of equilibration (Supplementary Fig. 7). For each independent replicate, the mean of the Cγ D325 - Cβ S47 distance was calculated over 2.2 μs. For each condition, the average over the replicates was plotted with error bars representing the s.e.m. (Supplementary. Fig. 7). The flexibility of D325 was quantified by calculating the root-mean-square fluctuation (RMSF) of the side-chain atoms of D325 using an in-house script (Supplementary Fig. 7). Statistical significance was determined using the Mann-Whitney U test.

Data Availability

All data generated or analyzed during this study are included in this published article and its Supplementary Information. Crystallographic coordinates and structure factors for the Fab45D8 complex have been deposited in the Protein Data Bank under accession code 6W4V. Coordinates for Fab45D8-FPN complex have been deposited in the Protein Data Bank under accession code 6W4S and the maps have been deposited in the Electron Microscopy Data Bank under accession code 21539. Coordinates for the FPN-Co^{2+}-hepcidin-Fab45D8 complex have been deposited in the Protein Data Bank under accession code 6WBV and the maps have been deposited in the Electron Microscopy Data Bank under accession code 21599.

Conflict of Interest

Tara Arvedson is employed by Amgen and reports Amgen stock. None of the other authors report conflicts of interest.

REFERENCES

1. Drakesmith, H., Nemeth, E. & Ganz, T. Ironing out Ferroportin. *Cell Metab.* **22**, 777–787 (2015).
2. Donovan, A. *et al.* The iron exporter ferroportin/Slc40a1 is essential for iron homeostasis. *Cell Metab.* **1**, 191–200 (2005).
3. Donovan, A. *et al.* Positional cloning of zebrafish ferroportin1 identifies a conserved vertebrate iron exporter. *Nature* **403**, 776–781 (2000).
4. Knutson, M. D., Oukka, M., Koss, L. M., Aydemir, F. & Wessling-Resnick, M. Iron release from macrophages after erythrophagocytosis is up-regulated by ferroportin 1 overexpression and down-regulated by hepcidin. *Proc. Natl. Acad. Sci. U. S. A.* **102**, 1324–1328 (2005).
5. Ward, D. M. & Kaplan, J. Ferroportin-mediated iron transport: expression and regulation. *Biochim. Biophys. Acta* **1823**, 1426–1433 (2012).
6. Aschemeyer, S. *et al.* Structure-function analysis of ferroportin defines the binding site and an alternative mechanism of action of hepcidin. *Blood, The Journal of the American Society of Hematology* **131**, 899–910 (2018).
7. Nemeth, E. *et al.* Hepcidin regulates cellular iron efflux by binding to ferroportin and inducing its internalization. *Science* **306**, 2090–2093 (2004).
8. De Domenico, I. *et al.* The molecular mechanism of hepcidin-mediated ferroportin down-regulation. *Mol. Biol. Cell* **18**, 2569–2578 (2007).
9. Qiao, B. *et al.* Hepcidin-induced endocytosis of ferroportin is dependent on ferroportin ubiquitination. *Cell Metab.* **15**, 918–924 (2012).
10. Ross, S. L. *et al.* Molecular mechanism of hepcidin-mediated ferroportin internalization requires ferroportin lysines, not tyrosines or JAK-STAT. *Cell Metab.* **15**, 905–917 (2012).
11. Roetto, A. *et al.* Mutant antimicrobial peptide hepcidin is associated with severe juvenile hemochromatosis. *Nat. Genet.* **33**, 21–22 (2003).
12. De Domenico, I. *et al.* The molecular basis of ferroportin-linked hemochromatosis. *Proc. Natl. Acad. Sci. U. S. A.* **102**, 8955–8960 (2005).

13. Drakesmith, H. *et al.* Resistance to hepcidin is conferred by hemochromatosis-associated mutations of ferroportin. *Blood* **106**, 1092–1097 (2005).

14. Roy, C. N. *et al.* Hepcidin antimicrobial peptide transgenic mice exhibit features of the anemia of inflammation. *Blood* **109**, 4038–4044 (2007).

15. Ganz, T. & Nemeth, E. The hepcidin-ferroportin system as a therapeutic target in anemias and iron overload disorders. *Hematology Am. Soc. Hematol. Educ. Program* **2011**, 538–542 (2011).

16. Manolova, V. *et al.* Oral ferroportin inhibitor ameliorates ineffective erythropoiesis in a model of β-thalassemia. *J. Clin. Invest.* (2019) doi:10.1172/JCI129382.

17. Witcher, D. R. *et al.* LY2928057, an antibody targeting ferroportin, is a potent inhibitor of hepcidin activity and increases iron mobilization in normal cynomolgus monkeys. (2013).

18. Crielaard, B. J., Lammers, T. & Rivella, S. Targeting iron metabolism in drug discovery and delivery. *Nat. Rev. Drug Discov.* **16**, 400–423 (2017).

19. Vlasveld, L. T. *et al.* Twenty Years of Ferroportin Disease: A Review or An Update of Published Clinical, Biochemical, Molecular, and Functional Features. *Pharmaceuticals* **12**, (2019).

20. Nemeth, E. *et al.* The N-terminus of hepcidin is essential for its interaction with ferroportin: structure-function study. *Blood* **107**, 328–333 (2006).

21. Jordan, J. B. *et al.* Hepcidin revisited, disulfide connectivity, dynamics, and structure. *J. Biol. Chem.* **284**, 24155–24167 (2009).

22. Bonaccorsi di Patti, M. C. *et al.* A structural model of human ferroportin and of its iron binding site. *FEBS J.* **281**, 2851–2860 (2014).

23. Taniguchi, R. *et al.* Outward- and inward-facing structures of a putative bacterial transition-metal transporter with homology to ferroportin. *Nat. Commun.* **6**, 8545 (2015).

24. Deshpande, C. N. *et al.* Calcium is an essential cofactor for metal efflux by the ferroportin transporter family. *Nat. Commun.* **9**, 3075 (2018).

25. Ross, S. L. *et al.* Identification of Antibody and Small Molecule Antagonists of Ferroportin-Hepcidin Interaction. *Front. Pharmacol.* **8**, 838 (2017).

26. Wu, S. *et al.* Fabs enable single particle cryoEM studies of small proteins. *Structure* **20**, 582–592

(2012).

27. Mitchell, C. J., Shawki, A., Ganz, T., Nemeth, E. & Mackenzie, B. Functional properties of human ferroportin, a cellular iron exporter reactive also with cobalt and zinc. *Am. J. Physiol. Cell Physiol.* **306**, C450–9 (2014).

28. Guellec, J. *et al.* Molecular model of the ferroportin intracellular gate and implications for the human iron transport cycle and hemochromatosis type 4A. *FASEB J.* **33**, 14625–14635 (2019).

29. Sham, R. L. *et al.* Autosomal dominant hereditary hemochromatosis associated with a novel ferroportin mutation and unique clinical features. *Blood Cells Mol. Dis.* **34**, 157–161 (2005).

30. Schimanski, L. M. *et al.* In vitro functional analysis of human ferroportin (FPN) and hemochromatosis-associated FPN mutations. *Blood* **105**, 4096–4102 (2005).

31. Viprakasit, V. *et al.* Molecular Diagnosis of the First Ferroportin Mutation (C326Y) in the Far East Causing a Dominant Form of Inherited Iron Overload. (2004).

32. Mayr, R. *et al.* Identification of mutations in SLC40A1 that affect ferroportin function and phenotype of human ferroportin iron overload. *Gastroenterology* **140**, 2056–63, 2063.e1 (2011).

33. Tortosa, V., di Patti, M. C. B., Brandi, V., Musci, G. & Polticelli, F. An improved structural model of the human iron exporter ferroportin. Insight into the role of pathogenic mutations in hereditary hemochromatosis type 4. *Bio-Algorithms and Med-Systems* **13**, 215–222 (2017).

34. Wallace, D. F., Clark, R. M., Harley, H. A. J. & Nathan Subramaniam, V. Autosomal dominant iron overload due to a novel mutation of ferroportin1 associated with parenchymal iron loading and cirrhosis. *Journal of Hepatology* vol. 40 710–713 (2004).

35. Njajou, O. T. *et al.* A mutation in SLC11A3 is associated with autosomal dominant hemochromatosis. *Nat. Genet.* **28**, 213–214 (2001).

36. Arden, K. E. *et al.* A novel mutation in ferroportin1 is associated with haemochromatosis in a Solomon Islands patient. *Gut* **52**, 1215–1217 (2003).

37. Zhang, W. *et al.* A novel SLC40A1 p.Y333H mutation with gain of function of ferroportin: A recurrent cause of haemochromatosis in China. *Liver Int.* **39**, 1120–1127 (2019).

38. Létocart, E. *et al.* A novel missense mutation in SLC40A1 results in resistance to hepcidin and

confirms the existence of two ferroportin-associated iron overload diseases. *Br. J. Haematol.* **147**, 379–385 (2009).

39. Callebaut, I. *et al.* Comprehensive functional annotation of 18 missense mutations found in suspected hemochromatosis type 4 patients. *Hum. Mol. Genet.* **23**, 4479–4490 (2014).
40. Preza, G. C. *et al.* Minihepcidins are rationally designed small peptides that mimic hepcidin activity in mice and may be useful for the treatment of iron overload. *J. Clin. Invest.* **121**, 4880–4888 (2011).
41. Rivard, S. R. *et al.* Autosomal dominant reticuloendothelial iron overload (HFE type 4) due to a new missense mutation in the FERROPORTIN 1 gene (SLC11A3) in a large French-Canadian family. *Haematologica* **88**, 824–826 (2003).
42. Raszeja-Wyszomirska, J., Caleffi, A., Milkiewicz, P. & Pietrangelo, A. Ferroportin-related haemochromatosis associated with novel Y64H mutation of the SCL40A1 gene. *Prz Gastroenterol* **9**, 307–309 (2014).
43. Clark, R. J. *et al.* Understanding the structure/activity relationships of the iron regulatory peptide hepcidin. *Chem. Biol.* **18**, 336–343 (2011).
44. Smythe, M. L. *et al.* Hepcidin analogues and uses thereof. *US Patent* (2017).
45. Bourne, G. T., Smythe, M. L., Frederick, B. T. & Vink, S. Hepcidin and mini-hepcidin analogues and uses therof. *US Patent* (2020).
46. Galesloot, T. E. *et al.* Serum hepcidin: reference ranges and biochemical correlates in the general population. *Blood* **117**, e218–25 (2011).
47. Nasr, M. L. *et al.* Covalently circularized nanodiscs for studying membrane proteins and viral entry. *Nat. Methods* **14**, 49–52 (2017).
48. Winter, G., Lobley, C. M. C. & Prince, S. M. Decision making in xia2. *Acta Crystallogr. D Biol. Crystallogr.* **69**, 1260–1273 (2013).
49. Kabsch, W. XDS. *Acta Crystallogr. D Biol. Crystallogr.* **66**, 125–132 (2010).
50. McCoy, A. J. *et al.* Phaser crystallographic software. *J. Appl. Crystallogr.* **40**, 658–674 (2007).
51. Aleman, F. *et al.* Immunogenetic and structural analysis of a class of HCV broadly neutralizing antibodies and their precursors. *Proc. Natl. Acad. Sci. U. S. A.* **115**, 7569–7574 (2018).

52. Emsley, P. & Cowtan, K. Coot: model-building tools for molecular graphics. *Acta Crystallogr. D Biol. Crystallogr.* **60**, 2126–2132 (2004).

53. Adams, P. D. *et al.* PHENIX: a comprehensive Python-based system for macromolecular structure solution. *Acta Crystallogr. D Biol. Crystallogr.* **66**, 213–221 (2010).

54. Chen, V. B. *et al.* MolProbity: all-atom structure validation for macromolecular crystallography. *Acta Crystallogr. D Biol. Crystallogr.* **66**, 12–21 (2010).

55. Cote, L. J., Kim, F. & Huang, J. Langmuir- Blodgett assembly of graphite oxide single layers. *J. Am. Chem. Soc.* **131**, 1043–1049 (2009).

56. Palovcak, E. *et al.* A simple and robust procedure for preparing graphene-oxide cryo-EM grids. *J. Struct. Biol.* **204**, 80–84 (2018).

57. Wang, F. *et al.* Amino and PEG-amino graphene oxide grids enrich and protect samples for high-resolution single particle cryo-electron microscopy. *J. Struct. Biol.* **209**, 107437 (2020).

58. Mastronarde, D. N. SerialEM: A Program for Automated Tilt Series Acquisition on Tecnai Microscopes Using Prediction of Specimen Position. *Microsc. Microanal.* **9**, 1182–1183 (2003).

59. Zheng, S. Q. *et al.* MotionCor2: anisotropic correction of beam-induced motion for improved cryo-electron microscopy. *Nat. Methods* **14**, 331–332 (2017).

60. de la Rosa-Trevín, J. M. *et al.* Scipion: A software framework toward integration, reproducibility and validation in 3D electron microscopy. *J. Struct. Biol.* **195**, 93–99 (2016).

61. Punjani, A., Rubinstein, J. L., Fleet, D. J. & Brubaker, M. A. cryoSPARC: algorithms for rapid unsupervised cryo-EM structure determination. *Nat. Methods* **14**, 290–296 (2017).

62. Scheres, S. H. W. RELION: implementation of a Bayesian approach to cryo-EM structure determination. *J. Struct. Biol.* **180**, 519–530 (2012).

63. Rohou, A. & Grigorieff, N. CTFFIND4: Fast and accurate defocus estimation from electron micrographs. *J. Struct. Biol.* **192**, 216–221 (2015).

64. Asarnow, D., Palovcak, E. & Cheng, Y. *asarnow/pyem: UCSF pyem v0.5*. (2019). doi:10.5281/zenodo.3576630.

65. Grant, T., Rohou, A. & Grigorieff, N. cisTEM, user-friendly software for single-particle image

875 processing. *Elife* **7**, (2018).

876 66. Dang, S. *et al.* Cryo-EM structures of the TMEM16A calcium-activated chloride channel. *Nature* **552**,

877 426–429 (2017).

878 67. Rosenthal, P. B. & Henderson, R. Optimal determination of particle orientation, absolute hand, and

879 contrast loss in single-particle electron cryomicroscopy. *J. Mol. Biol.* **333**, 721–745 (2003).

880 68. Eswar, N. *et al.* Comparative protein structure modeling using MODELLER. *Curr. Protoc. Protein Sci.*

881 **Chapter 2**, Unit 2.9 (2007).

882 69. Goddard, T. D., Huang, C. C. & Ferrin, T. E. Visualizing density maps with UCSF Chimera. *J. Struct.*

883 *Biol.* **157**, 281–287 (2007).

884 70. Barad, B. A. *et al.* EMRinger: side chain-directed model and map validation for 3D cryo-electron

885 microscopy. *Nat. Methods* **12**, 943–946 (2015).

886 71. Betz, R. *Dabble*. (2017). doi:10.5281/zenodo.836914.

887 72. Olsson, M. H. M., Søndergaard, C. R., Rostkowski, M. & Jensen, J. H. PROPKA3: Consistent

888 Treatment of Internal and Surface Residues in Empirical pKa Predictions. *J. Chem. Theory Comput.*

889 **7**, 525–537 (2011).

890 73. Søndergaard, C. R., Olsson, M. H. M., Rostkowski, M. & Jensen, J. H. Improved Treatment of

891 Ligands and Coupling Effects in Empirical Calculation and Rationalization of pKa Values. *J. Chem.*

892 *Theory Comput.* **7**, 2284–2295 (2011).

893 74. Morozenko, A. & Stuchebrukhov, A. A. Dowser , a new method of hydrating protein structures.

894 *Proteins: Structure, Function, and Bioinformatics* vol. 84 1347–1357 (2016).

895 75. Lomize, M. A., Lomize, A. L., Pogozheva, I. D. & Mosberg, H. I. OPM: orientations of proteins in

896 membranes database. *Bioinformatics* **22**, 623–625 (2006).

897 76. Klauda, J. B. *et al.* Update of the CHARMM all-atom additive force field for lipids: validation on six

898 lipid types. *J. Phys. Chem. B* **114**, 7830–7843 (2010).

899 77. Huang, J. *et al.* CHARMM36m: an improved force field for folded and intrinsically disordered

900 proteins. *Nat. Methods* **14**, 71–73 (2017).

901 78. Beglov, D. & Roux, B. Finite representation of an infinite bulk system: Solvent boundary potential for

computer simulations. *J. Chem. Phys.* **100**, 9050–9063 (1994).

79. Li, P., Roberts, B. P., Chakravorty, D. K. & Merz, K. M., Jr. Rational design of particle mesh Ewald compatible Lennard-Jones parameters for+ 2 metal cations in explicit solvent. *J. Chem. Theory Comput.* **9**, 2733–2748 (2013).
80. Case, D. A. *et al.* AMBER 2018; 2018. *University of California, San Francisco*.
81. Salomon-Ferrer, R., Götz, A. W., Poole, D., Le Grand, S. & Walker, R. C. Routine Microsecond Molecular Dynamics Simulations with AMBER on GPUs. 2. Explicit Solvent Particle Mesh Ewald. *J. Chem. Theory Comput.* **9**, 3878–3888 (2013).
82. Hopkins, C. W., Le Grand, S., Walker, R. C. & Roitberg, A. E. Long-Time-Step Molecular Dynamics through Hydrogen Mass Repartitioning. *J. Chem. Theory Comput.* **11**, 1864–1874 (2015).
83. Ryckaert, J.-P., Ciccotti, G. & Berendsen, H. J. C. Numerical integration of the cartesian equations of motion of a system with constraints: molecular dynamics of n-alkanes. *J. Comput. Phys.* **23**, 327–341 (1977).
84. Roe, D. R. & Cheatham, T. E., 3rd. PTRAJ and CPPTRAJ: Software for Processing and Analysis of Molecular Dynamics Trajectory Data. *J. Chem. Theory Comput.* **9**, 3084–3095 (2013).
85. Humphrey, W., Dalke, A. & Schulten, K. VMD: visual molecular dynamics. *J. Mol. Graph.* **14**, 33–8, 27–8 (1996).